Bulletin of Volcanology (2023) 85:39
https://doi.org/10.1007/s00445-023-01651-2

RESEARCH ARTICLE

Historical explosive activity of Mount Melbourne Volcanic Field (Antarctica) revealed by englacial tephra deposits

Paola Del Carlo[1] · Alessio Di Roberto[1] · Giuseppe Re[1] · Paul G. Albert[2] · Victoria C. Smith[3] · Gaetano Giudice[4] · Graziano Larocca[4] · Bianca Scateni[1,5] · Andrea Cannata[4,6]

Received: 28 February 2023 / Accepted: 13 May 2023
© The Author(s) 2023

Abstract

Five tephra layers named BRH1 to 5 were sampled in an ice cliff located on the north-eastern flank of Mount Melbourne (northern Victoria Land, Antarctica). The texture, componentry, mineralogy, and major and trace element compositions of glass shards have been used to characterize these layers. These properties suggest that they are primary fall deposits produced from discrete eruptions that experienced varying degrees of magma/water interaction. The major and trace element glass shard analyses on single glass shards indicate that Mount Melbourne Volcanic Field is the source of these tephra layers and the geochemical diversity highlights that the eruptions were fed by compositionally diverse melts that are interpreted to be from a complex magma system with a mafic melt remobilizing more evolved trachy-andesitic to trachytic magma pockets. Geochemical compositions, along with textural and mineralogical data, have allowed correlations between two of the englacial tephra and distal cryptotephra from Mount Melbourne, recovered within a marine sediment core in the Edisto Inlet (~ 280 km northeast of Mount Melbourne), and constrain the age of these englacial tephra layers to between the third and the fourth century CE. This work provides new evidence of the intense historical explosive activity of the Mount Melbourne Volcanic Field and better constrains the rates of volcanism in northern Victoria Land. These data grant new clues on the eruptive dynamics and tephra dispersal, and considerably expand the geochemical (major and trace elements) dataset available for the Mount Melbourne Volcanic Field. In the future, this will facilitate the precise identification of tephra layers from this volcanic source and will help define the temporal and spatial correlation between Antarctic records using tephra layers. Finally, this work also yields new valuable time-stratigraphic marker horizons for future dating, synchronization, and correlations of different palaeoenvironmental and palaeoclimatic records across large regions of Antarctica.

Keywords Antarctica · Mount Melbourne Volcanic Field · Explosive eruptions · Englacial tephra · Glass geochemistry · Historical eruptions

Editorial responsibility: J.L. Smellie

✉ Alessio Di Roberto
alessio.diroberto@ingv.it

Paola Del Carlo
paola.delcarlo@ingv.it

Giuseppe Re
giuseppe.re@ingv.it

[1] Istituto Nazionale di Geofisica e Vulcanologia, Sezione di Pisa, Via C. Battisti 53, 56125 Pisa, Italy

[2] Department of Geography, Swansea University, Singleton Park, Swansea SA2 8PP, UK

[3] Research Laboratory for Archaeology and the History of Art, University of Oxford, 1 South Parks Road, Oxford OX1 3TG, UK

[4] Istituto Nazionale di Geofisica e Vulcanologia, Osservatorio Etneo, Piazza Roma 2, 95125 Catania, Italy

[5] Dipartimento di Scienze Della Terra, Università di Pisa, 56126 Pisa, Italy

[6] Dipartimento di Scienze Biologiche, Geologiche e Ambientali, Università di Catania, Corso Italia 57, Catania 95125, Italy

Published online: 31 May 2023

Introduction

Tephra in Antarctic ice records (ice cores or blue ice) provide important sources of data for evaluating the history and evolution of Antarctic explosive volcanism. The typical absence of pyroclastic deposits at proximal locations on the flanks of the volcanoes, due to high rates of post-depositional erosion and/or remobilization and also (mainly) the extensive cover of snow and ice obscuring deposits on the volcanic centres, limits the reconstruction of past volcanic eruptions, including their timing, scale, and impact on the environment. This gap in knowledge can be overcome by the study of tephra and cryptotephra (not visible, highly disseminated, fine-grained tephra) at medial to distal sites, which are preserved and remain unaltered within the snow, transformed into glacial ice upon burial (Smellie 1999; Harpel et al. 2008; Iverson et al. 2017). In polar regions, and particularly in Antarctica, tephrochronological studies in ice cores and blue ice records have been well developed over recent decades (e.g. Narcisi et al. 2005; Kurbatov et al. 2006; Curzio et al. 2008; Iverson et al. 2014; Wolff et al. 2010; Narcisi et al. 2012; Severi et al. 2012; Kim et al. 2020; Nardin et al. 2021). Along with tephra included in marine sediment sequences (Hillenbrand et al. 2008; Del Carlo et al. 2015; Di Roberto et al. 2019; 2020; 2021a; b; 2023), tephra deposits in englacial sequences can help improve near-vent eruption records, in terms of both frequency/chronology of explosive volcanism, and magma chemical evolution through time, whilst facilitating advancements in dating, correlating, and synchronizing high-resolution climate and atmospheric composition records through the Late Quaternary (Narcisi and Petit 2021). In addition, tephrochronological correlations between different archives (e.g. ice and marine records), located at proximal and distal sites from an eruptive source, are greatly enhanced once a numerical age is obtained for tephra. Specifically, the correlation of two tephra layers allows the age-transfer from one site to another by the simple use of stratigraphy, heightening tephrochronology to an age-equivalent dating method (Lowe 2011).

Mount Melbourne is an active volcano in northern Victoria Land, Antarctica, and future activity on the volcano would pose a significant tephra fall risk to nearby scientific stations, e.g. Mario Zucchelli Station (Italian), Jang Bogo (Korea), Gondwana (Germany), and the new China Antarctic research base (Fig. 1a), as well as to Austral hemisphere air traffic. Therefore, a good knowledge of the recent volcanic activity of this volcano is important to better evaluate the possible volcanic hazards (Geyer 2021).

The earliest investigations on Mount Melbourne began at the end of the 1960s whereas the first geophysical observations started in 1988 by Italian National Antarctic Research Program (PNRA); since then no eruptive activity has been observed at this volcano. The age of the most recent eruption is proposed by Lyon (1986) who performed the stable isotope analysis of two snow profiles sampled on Mount Melbourne at ca. 2000 m of altitude and on the Campbell Glacier obtaining snow accumulation rates of 0.5–2.2 m/a. Using these data, the author derived the age of englacial ash layers outcropping in an ice cliff at ca. 1200 m of altitude on the western slope of Mount Melbourne and photographed in 1965 by Adamson and Cavaney (1967). They roughly estimated the depth of snow from the surface to the first major ash layer to be between 29 and 36 m and, considering an accumulation rate of 0.5 ± 0.16 m/a, the last major eruption should have occurred between 1862 and 1922 AD. Although this method has several limitations (e.g. the lack of direct measurement of the snow thickness, or the detailed study of snow profile aimed at identifying possible hiatus or erosion surfaces), it does provide an estimate of the age of the latest eruptive activity of Mount Melbourne. Unfortunately, the englacial tephra layers described in Lyon (1986) and Adamson and Cavaney (1967) were never sampled nor characterized in their textural and geochemical features because the outcrop did not allow safe sampling.

During the 2017 austral summer, the ICE-VOLC project (PNRA) facilitated new geological surveys around Mount Melbourne which revealed the occurrence of multiple englacial volcanic ash layers in an ice cliff located on the northeast flank of the volcano at ca. 800 m of altitude, very close to Baker Rock location (Gambino et al. 2021; Fig. 1). The better accessibility of the outcrop allowed the sampling of tephra and the measurements of the thickness between the different ash layers.

In this paper, we present data on the texture, mineral phases, and major and trace element geochemical data performed on single glass shards analyzed via Electron Probe Microanalysis (EMPA) and Laser Ablation Inductively Coupled Plasma Mass Spectrometry (LA-ICP-MS) of five englacial tephra layers sampled for the first time from the north-eastern flank of Mount Melbourne. Geochemical data indicate that the tephra layers are derived from Mount Melbourne explosive activity. The texture of the particles and their morphological features were important for clues to the style of the eruptions and fragmentation mechanisms. In addition, geochemical fingerprints of englacial tephra have allowed their correlations and dating with cryptotephra layers recently found in marine sediments in Edisto Inlet near Cape Hallett (Di Roberto et al. 2023), highlighting that Mount Melbourne has been very active during historical times.

Geological setting

Mount Melbourne stands as a 2732-m-high stratovolcano with a basal diameter of about 21–24 km on the coast of northern Victoria Land, between Wood Bay and Terra Nova Bay, in Antarctica (Fig. 1b). The Mount Melbourne

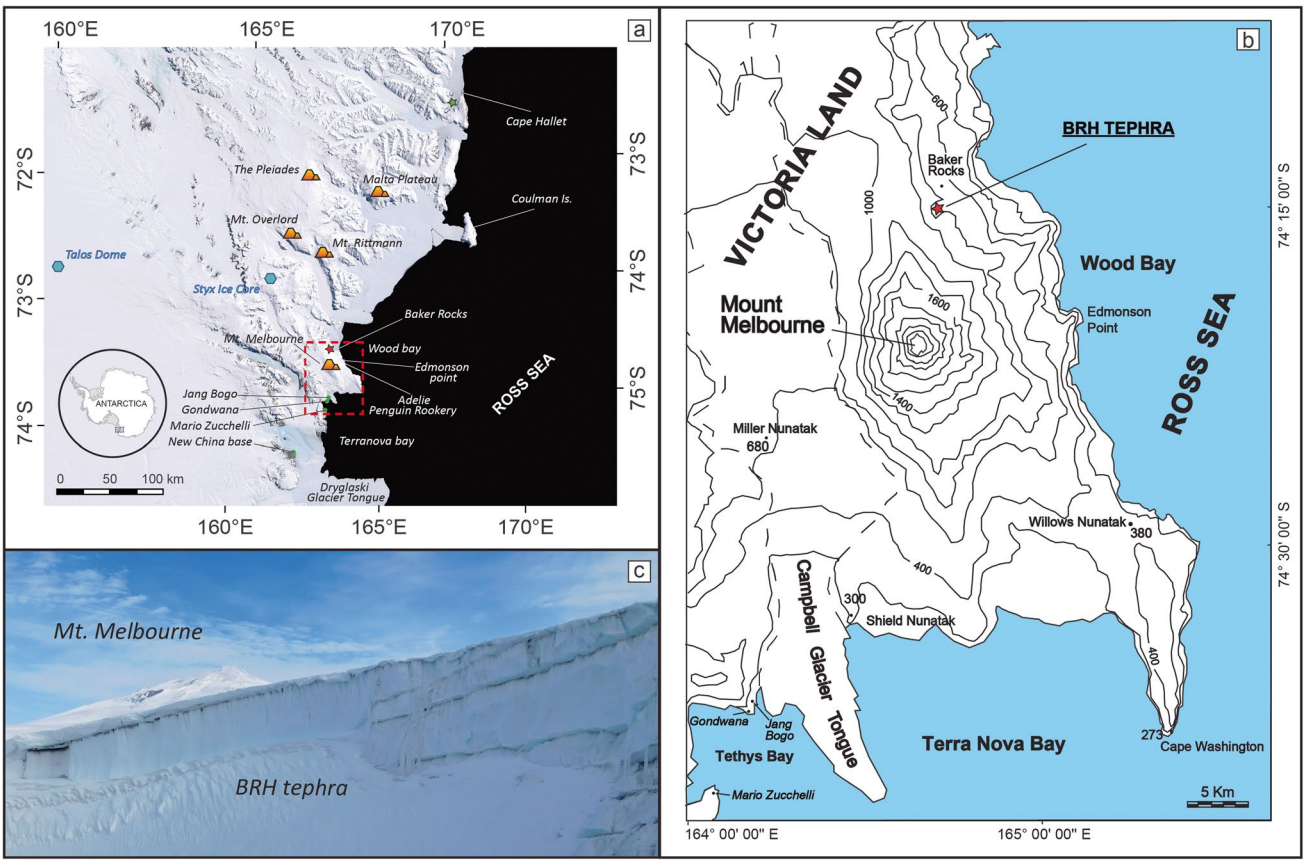

Fig. 1 (**a**) Map of the volcanoes in northern Victoria Land. The location of the studied outcrop is labelled with a red star whereas the location of the marine sediment core TR17-08 in Edisto Inlet (Di Roberto et al. 2023) and of the deep ice cores at Talos Dome and Styx glacier are annotated with a green star and blue hexagons, respectively. Green dots indicate the location of the permanent scientific bases. The red box outlines the area of the topographic map in (**b**) that illustrates Mount Melbourne and locations of the BRH sections. (**c**) Picture of the studied outcrop where the BRH tephra layers are exposed, Mount Melbourne in the background

volcano also includes several parasitic cones and secondary vents located on the flank of the main edifice (Smellie et al. 2023). The main volcano edifice shows a gentle shape with undissected flanks, apart from a possible slump scar on the east side (Giordano et al. 2012), and a well-formed ice-filled crater ca. 700 m in diameter that Armienti et al. (1991) interpreted as a summit caldera. It is largely covered by snow and ice except for the summit region where rock outcrops extend downslope on the east side to ca. 1800 m. The Mount Melbourne Volcanic Field (MMVF), together with The Pleiades, Mount Overlord, Mount Rittmann, and the Malta Plateau volcanoes, is part of the Melbourne Volcanic Province within the McMurdo Volcanic Group (Smellie and Rocchi 2021). A synthesis of MMVF volcanic history was reported by Giordano et al. (2012) and Smellie et al. (2023) based on stratigraphic and volcanological studies, geochemical data, and age determinations. According to recent updates based on radioisotopic ages, the MMVF volcanism began in the Late Miocene (c. 12.5 Ma for centres in the north by Tinker Glacier) but developed mainly from the Pliocene (c. 4 Ma; Smellie et al. 2023) particularly after c. 3 million years ago (Rocchi and Smellie 2021 and references therein). The activity can be subdivided into different evolution stages: (i) the older Cape Washington shield volcano (Late Miocene-Late Pliocene), (ii) the Random Hills Period (Lower-Middle Pleistocene), (iii) the Shield Nunatak Period (Middle Pleistocene), and (iv) the Mount Melbourne Period (Upper Pleistocene-present; Giordano et al. 2012; Smellie et al. 2023).

The oldest deposit that can be linked directly to an eruption of the Mount Melbourne stratovolcano, re-dated as 115 ka by Smellie et al. (2023) at Edmonson Point, is a trachytic ignimbrite. This was emplaced during a large Plinian eruption and indicates the formation of a crustal magma chamber during the recent Mount Melbourne stage (Giordano et al. 2012). Subsequently, the Adelie Penguin Rookery lava field succession was produced comprising alkali basaltic, hawaiitic, and subordinate benmoreitic lavas, scoria cones, and spatter cones that are dated at 90.7 ± 19.0 ka. (Giordano et al. 2012).

Evidence of more recent activity, based on tephrostratigraphic analysis and ^{40}Ar-^{39}Ar dating of proximal pyroclastic sequence exposed on the Mount Melbourne summit, indicates there were at least four Strombolian or Vulcanian style to sub-Plinian/Plinian eruptions during the Late Pleistocene to Holocene (Del Carlo et al. 2022). The most intense of these eruptions was a sub-Plinian to Plinian eruption that yielded an age < 17.8 ka (13.5 ± 4.3 ka). Furthermore, three trachytic cryptotephra with glass compositions similar to Mount Melbourne products were found intercalated in marine sediments of Edisto Inlet, near Cape Hallett (Di Roberto et al. 2023). These cryptotephra layers were interpreted as derived from historic explosive eruptions of Mount Melbourne that occurred between 1615 cal. years BP and 1677 cal. years BP, i.e. between the third and fourth century CE (Di Roberto et al. 2023).

Presently, the Mount Melbourne volcano is quiescent with thermal anomalies, including noticeable steaming or fumarolic activity both in the crater and on the north-western side of the volcano. These emissions of steam and volcanic gas have produced several ice towers and a complex network of ice caves, as recently reported after geochemical surveys in the frame of the ICE-VOLC project (Gambino et al. 2021).

Material and methods

During the XXXII Italian Antarctic Expedition in 2017, the area surrounding Mount Melbourne was aerially surveyed by helicopter flights. A series of dark, sub-horizontal englacial tephra layers were found exposed along a ca. 50-m-high ice cliff located on the north-eastern flank of the volcano at about 800 m of altitude close to Baker Rock (74.24096 S, 164.72032 E; red star in Fig. 1). Five sub-horizontal tephra layers, named BRH1 to 5 (from the top to the bottom), were distinguished and sampled by the Italian alpine climbing guides (Fig. 2). Tephra layers are between 10 and 20 cm thick and are each separated by 1.5 to 7.5 m of ice (Fig. 2). Each sample is collected the "bulk" of the tephra layer and represents the whole unit; unfortunately, due to the extreme sampling conditions, it was not possible to sub-sample different stratigraphic heights within each unit. The tephra samples were recovered still embedded in the ice, which was then melted to recover the clastic fraction.

Sample preparation was carried out at laboratories of Istituto Nazionale di Geofisica e Vulcanologia, Sezione di Pisa (INGV-Pisa). Samples were washed with deionized water in an ultrasonic bath to remove impurities, dried at 60 °C, mounted with epoxy resin in 1-in. stubs, polished, and prepared for textural and geochemical analyses. Textures, components, and mineral assemblages of each tephra were studied with an optical microscope and a scanning electron microscope (SEM) Zeiss EVO MA and images of 3D silhouettes and 2D cross-sections have been collected in secondary (SE) and back-scattered (BSE) electrons mode, respectively. The major and minor elements glass composition of samples was determined using a JEOL 8600 wavelength-dispersive electron microprobe equipped with four spectrometers at the Research Laboratory for Archaeology and the History of Art, the University of Oxford (operating conditions: 15-kV accelerating voltage, 6-nA beam current, and a beam diameter of 10 μm). The JEOL 8600 electron microprobe was calibrated with a suite of appropriate mineral standards; peak count times were 30 s for all elements except Mn (40 s), Na (12 s), Cl (50 s), and P (60 s). The PAP absorption correction method was used for quantification. Reference glasses from the Max Planck Institute (MPI-DING suite; Jochum et al. 2006) bracketing the possible chemistries were also analyzed. These included felsic [ATHO-G (rhyolite)], through intermediate [StHs6/80-G (andesite)] to mafic [GOR132-G (komatiite)] glasses. All glass data have been normalized to 100% for comparative purposes. Uncertainties are typically < ± 0.8% RSD for Si; ~ ± 5% for most other

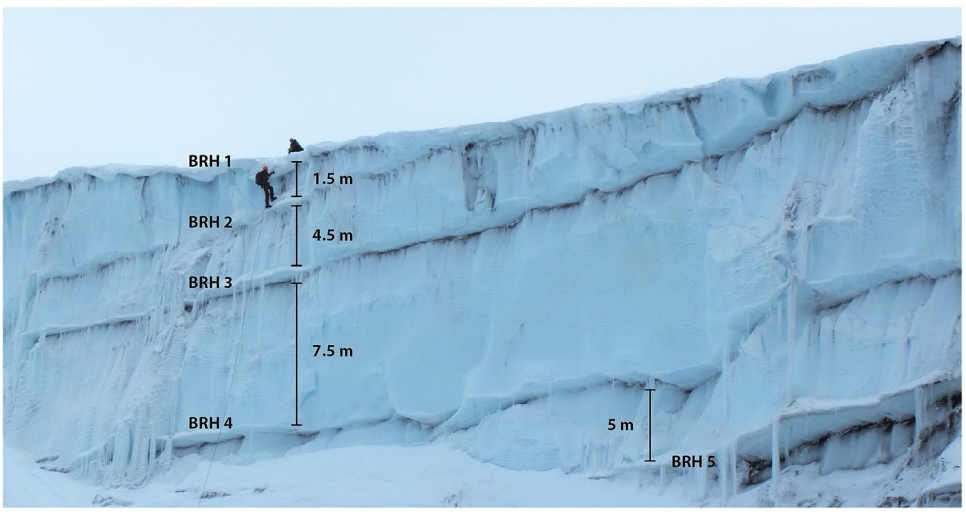

Fig. 2 Picture of the glacier cliff where BRH tephra layers are exposed, taken during the sampling performed by the Italian alpine guides. On the picture are annotated the five englacial tephra and the ice thickness between them

major elements, except for the low abundance elements, for instance Ti (~ ± 7%) and Mn (~ ± 30%).

Trace elements analysis of volcanic glass was performed using an Agilent 8900 triple quadrupole ICP-MS (ICP QQQ) coupled to a Resonetics 193 nm ArF excimer laser-ablation in the Department of Earth Sciences, Royal Holloway, University of London. Full analytical procedures used are reported in Tomlinson et al. (2010). Spot sizes 20 and 25 mm were used depending on the vesicularity, crystal content, and ultimately the size of available glass surfaces. The repetition rate was 5 Hz, with a count time of 40 s on the sample, and 40 s on the gas blank to allow the subtraction of the background signal. Blocks of eight or nine glass shards and one MPI-DING reference glass were bracketed by the NIST612 glass calibration standard (GeoREM 11/2006). In addition, MPI-DING reference glasses were used to monitor analytical accuracy (Jochum et al. 2005). The internal standard applied was ^{29}Si (determined by the EMPA analysis). Where individual shards were arranged into a grid formation across an epoxy mount, they are given a unique row (A, B, C) and shard number (1, 2, 3). In these instances, the grain-specific ^{29}Si content was applied as the internal standard. Where tephra samples were mounted in epoxy mounts without shard mapping, average ^{29}Si contents for the appropriate compositional groupings within the tephra deposit, determined based on EMPA analysis, were applied as the internal standard to the individual glass shards ablated. Internal standard values applied to individual shard ablations are provided in the Supplementary Information. LA-ICP-MS data reduction was performed in Microsoft Excel. Accuracies of LA-ICP-MS analyses of MPI-DING glass standards ATHO-G and StHs6/80-G were typically < 5%. Full glass datasets and MPI-DING standard glass analyses are provided in Supplemental Information.

Results

Texture and components of tephra layers

BRH samples are similar in terms of components, comprising a range of clasts with different textures ranging from dense to highly vesicular and glassy to microlite-rich (Figs. 3 and 4a–e). The morphology of juvenile clasts ranges from equant with rounded vesicles (Fig. 4f) to fluidal with elongated tubular vesicles (Fig. 4g, h). Dense poorly vesicular juveniles display features such as stepped surfaces and hackle lines, quenching cracks, and pitted surfaces (Fig. 4l, m), similar to the glassy shards that range from blocky to platy (Fig. 4i, n).

Overall, the grain size, scarcity of non-volcanic detrital material, and unabraded pristine shapes of the clasts indicate that these decimetre-thick layers are emplaced as primary fallout deposits. Extremely fragile particles such as glass fibres (Pele's hair) survived, and the external morphology of vesicular particles preserves pristine elements like fragile glass fibres, glass tips, spiny glass edges (Figs. 3 and 4), or glass coatings around magmatic crystals. Particles do not exhibit surficial alteration textures due to weathering, surface abrasion, or rounding. Lithic or detrital fragments are also scarce. All these features along with the geochemical fingerprints (see next paragraph) indicate very minor or no aeolian remobilization, re-sedimentation, or other transport after the deposition from the volcanic plume. Moreover, the layers occur close to the surface of the ice cover and well above the glacier bed, hence are unlikely to be glacier bedload brought to the surface by shearing.

As mentioned in the "Material and methods" section, the studied material comprises "bulk" samples of each tephra layer. Possible internal stratifications resulting from variations in eruptive style, energy, dynamics, magma reflected by changes in the glass composition, grain size, componentry, etc. were lost.

BRH1 tephra is the uppermost tephra exposed at the top of the ice cliff. It is made of coarse to very fine ash (Fig. 4a) and comprises two discrete particle populations differing in colour, shape, and texture. The first population, which is the more abundant, consists of shiny, black to dark brown, vesicular glassy clasts (Fig. 3a and g) with spiny to fluidal shapes (Fig. 3d), volcanic glass fibres, and glass droplets (Pele's hair and tears; Fig. 3c) and minor amounts of grey, dense, and blocky clasts (Fig. 3b). Often, particles with fluidal shapes are bounded by sharp-planar breakage surfaces (Fig. 3g). Fluidal clasts (Fig. 3a) are usually glassy aphyric to microlite-poor, poorly to moderately vesicular with spherical vesicles. Blocky clasts (Fig. 3b) are almost non-vesicular to very poorly vesicular with abundant microlites and microphenocrysts of andesine plagioclase (up to 60 µm), Fe-augite clinopyroxene (up to 30 µm), olivine (~ Fo_{45}; up to 10 µm), Fe-Ti oxides (up to 10 µm), and rare apatite (up to 10 µm). Also, crystals (up to ca. 250 µm) of plagioclase, olivine, and clinopyroxene occur coated in a dark glass.

The second particle population represents approximately 30% of the sample and has a finer grain size (fine ash). Particles comprise white to pale yellow, highly vesicular pumice fragments, and nearly transparent glass shards (Fig. 4a). Pumice fragments often show elongated to tubular vesicles (Fig. 3f), and bear within an aphyric groundmass abundant labradorite plagioclase (up to 80 µm) and olivine (~ Fo_{75}; up to 30 µm) with rare Mg-augite clinopyroxene (up to 20 µm) and Mg-chromite spinel (up to 10 µm). Lithic clasts are scarce in BRH1 tephra and consist of reddish or altered volcanic rocks (Fig. 3e).

BRH2 tephra is a poorly sorted lapilli (up to 4 mm) and ash (Fig. 4b) layer. It is predominantly composed of black/dark brown, shiny, vesicular glass fragments with spiny and

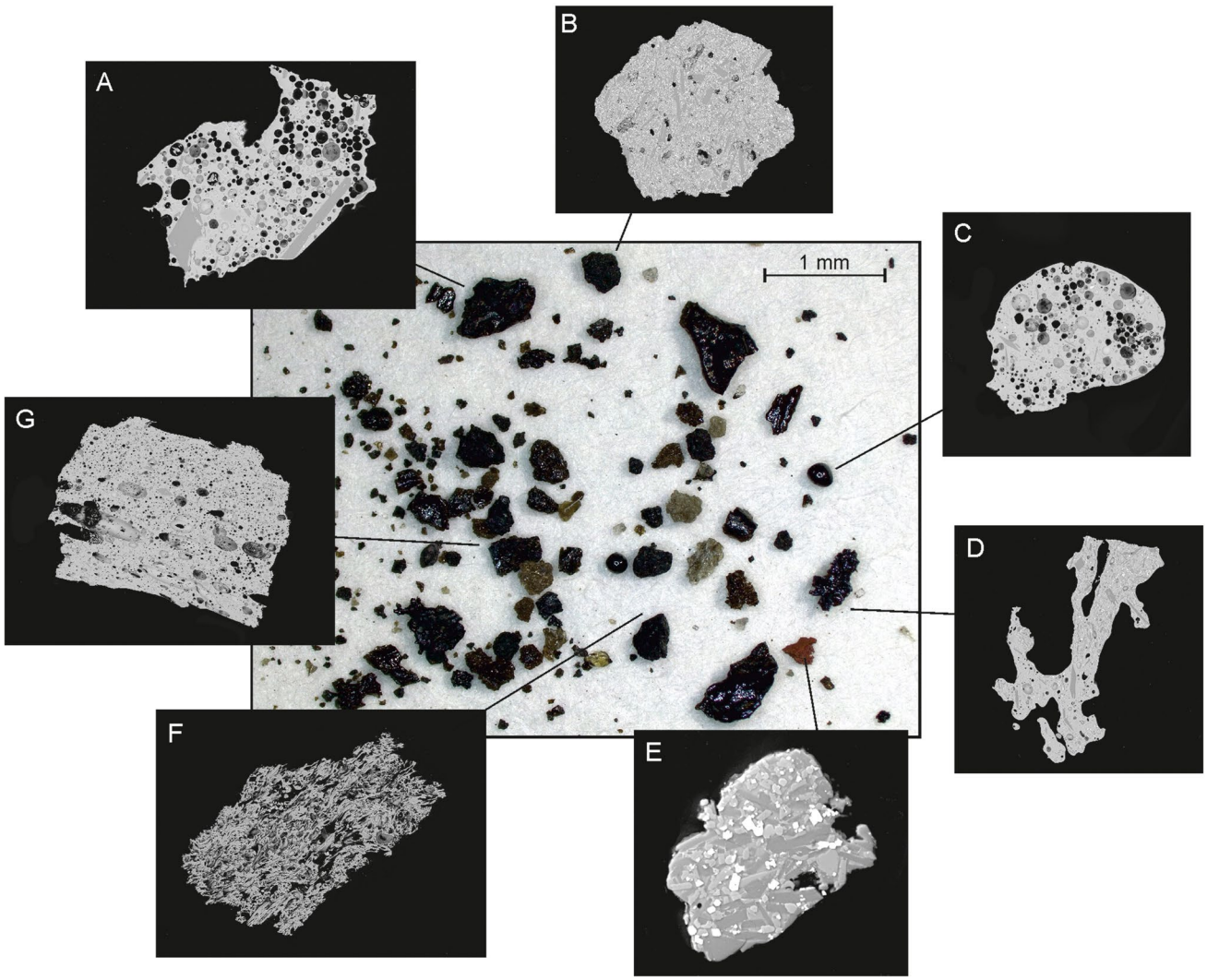

Fig. 3 Optical stereo-microscope images of the BRH4 ash. Images in the small boxes represent the different types of components: (**A**) vesicular; (**B**) blocky; (**C**) Pele's tear; (**D**) spiny fluidal; (**E**) lithic clast; (**F**) pumice; (**G**) vesicular fragment with sharp-planar breakage surface

fluidal shapes again often bounded by sharp-planar breakage surfaces (Fig. 3d), Pele's hair and tears, highly vesicular fragments, and grey dense, blocky clasts. Fluidal clasts (Fig. 4b) have glassy groundmass with spherical to elliptical vesicles and contain abundant microlites of andesine to oligoclase plagioclase (up to 50 µm), Fe-rich olivine (~ Fo_{35}; up to 15 µm), Fe-augite clinopyroxene (up to 30 µm), and Fe-Ti oxides (~ 10 mm). Grey dense and blocky clasts (Fig. 4b) are porphyritic with microphenocrysts of oligoclase to anorthoclase feldspar, Fe-augite, and Fe-Ti oxides within a glassy to microcrystalline groundmass. Tubular pumice fragments and bubble wall glass shards are abundant in the fine-grained, fine ash-sized portion of the deposit. Pumices have a glassy groundmass sometimes with acicular microlites of anorthitic feldspar. Scarce lithic clasts consist of reddish, altered volcanic rocks and intrusive rock fragments. Loose crystals of anorthoclase, clinopyroxene, and fayalite are abundant.

BRH3 tephra (Fig. 4c) is fine ash, with scarce scoriaceous fine lapilli, made of black to dark brown, shiny, poorly to moderately vesicular, fluidal glass particles (Fig. 4g) and grey, blocky fragments (Fig. 4n). Dark glass-coated crystals of plagioclase, clinopyroxene, and olivine are also abundant. Fluidal clasts are moderately vesicular, mainly with rounded tubular vesicles (Fig. 4g), and have glassy groundmass with phenocrysts of oligoclase plagioclase (up to 250 µm) and Fe-augite clinopyroxene (up to 350 µm); accessory minerals are anorthoclase feldspar (~ 90 µm), olivine (~ Fo_{20}; ~ 25 µm), Fe-Ti oxides (~ 15 µm), and apatite (~ 45 µm). Blocky fragments are poorly vesicular with abundant microlites of plagioclase, clinopyroxene, olivine, and Fe-Ti oxides. Pale yellow to white fibrous pumiceous clasts are also abundant in BRH3 tephra. Pumice fragments are mostly aphyric, with rare microphenocrysts of plagioclase and Fe-Ti oxides within a glassy highly vesicular groundmass with elongated

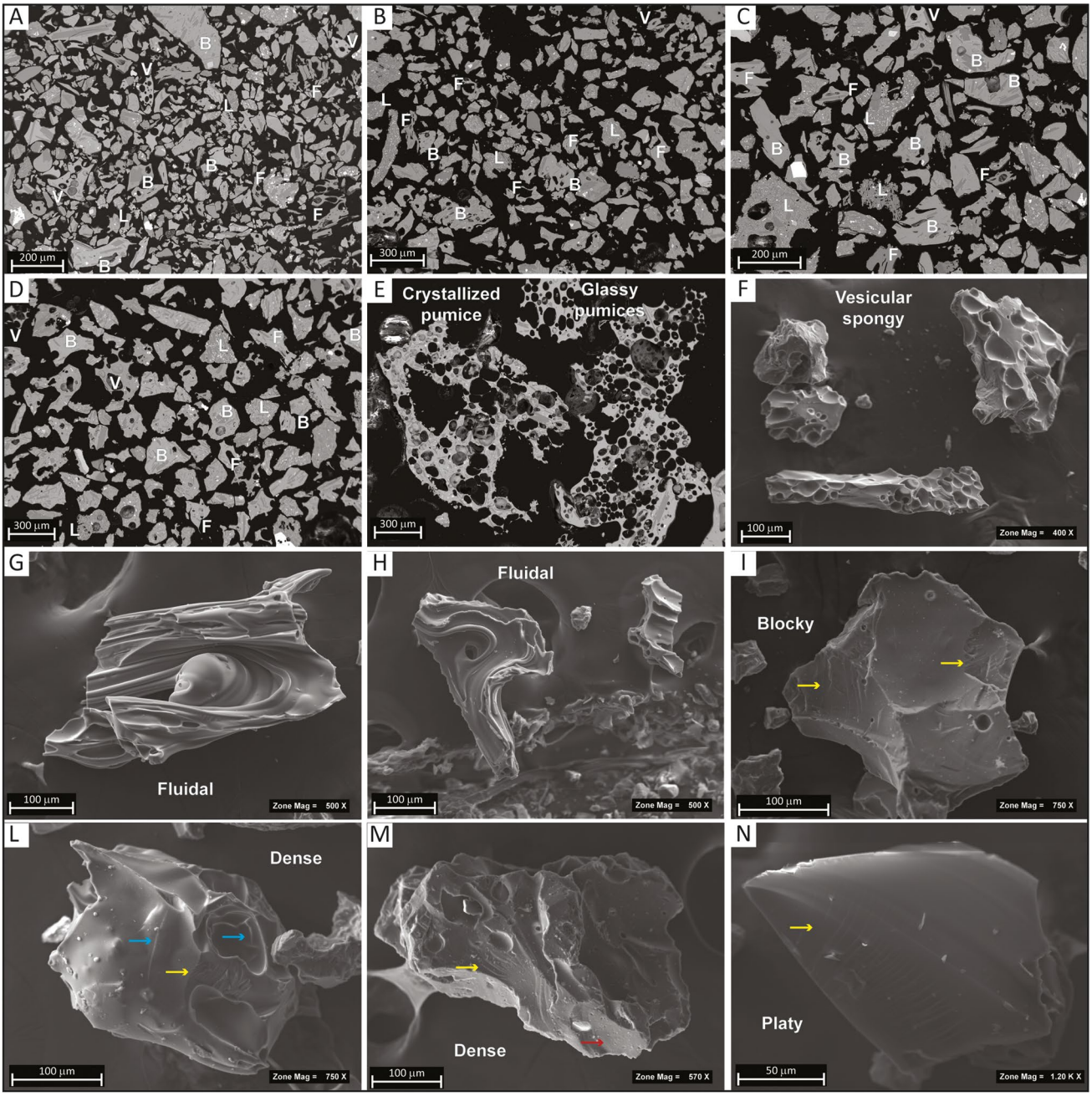

Fig. 4 Back-scattered electron (BSE) images of the studied tephra: (**A**) BRH1; (**B**) BRH2; (**C**) BRH3; (**D**) BRH4; (**E**) BRH5. Letters annotated within these five pictures represent the different types of components: B—blocky; F—fluidal; L—lithic clast; V—vesicular pumice fragment. Secondary electron images (F–N) of 3D silhouettes of selected clasts illustrating the morphology of magmatic (**F**–**H**) and phreatomagmatic (**I**–**N**) juvenile clasts. Yellow arrows indicate stepped features and hackle marks, blue arrows point at branching quenching cracks, and the red arrow highlights pitted surfaces

vesicles. Lithic clasts consist of red, oxidized lava fragments and altered tuffaceous rock fragments.

BRH4 tephra (Fig. 4d) is a very poorly sorted lapilli (up to 2 mm) to very fine ash layer. The sample is almost completely formed by black, shiny, spiny glass fragments and Pele's hair and tears, grey, dense and blocky clasts, and glass fragments (Fig. 4i). Golden-coloured, moderately vesicular glassy fragments are also present. Fluidal clasts (Fig. 4h) and golden vesicular fragments have porphyritic texture, with microphenocrysts of andesine plagioclase (~ 100 µm), olivine (~ Fo_{50}; ~ 20 µm), Fe-Ti oxides (~ 10 µm), within a glassy groundmass with rounded vesicles. The grey blocky particles (Fig. 4d) are highly porphyritic with abundant microphenocrysts of oligoclase plagioclase (~ 80 µm), Fe-Ti oxides

(~45 μm), and olivine (~Fo_{45}; ~40 μm), and subordinate anorthoclase/sanidine feldspar (~30 μm), Fe-augite clinopyroxene (~40 μm), and apatite (~25 μm), within a microlite-rich glassy groundmass. Many clasts show truncated shapes. Loose crystals of plagioclase, clinopyroxene, and olivine are abundant. Lithic clasts comprise lava and tuff fragments. A minor quantity of whitish, spongy pumice clasts is also present in the fine ash-sized fraction of the deposit. Pumice particles are aphyric and often present altered groundmass.

BRH5 tephra (Fig. 4e) is a very poorly sorted fine lapilli (up to 2 mm) to a fine ash layer. It comprises dark brown to black and shiny, vesicular glass fragments with spiny (Fig. 4i), fluidal, and blocky shapes, glass shards, and a few grey dense blocky clasts. Dense clasts are poorly vesicular, with spaced rounded to amoeboid vesicles, and porphyritic, with abundant microphenocrysts of labradorite plagioclase (up to 140 μm), olivine (~Fo_{60}; ~50 μm), Fe-Ti oxides (~30 μm), within a glassy groundmass with abundant microlites of plagioclase, Fe-rich olivine, Fe-augite clinopyroxene (up to 15 μm), and rare apatite (~10 μm). Clear to light grey pumice fragments are also abundant (ca. 20%). Pumices are highly vesicular with rounded and non-collapsed to tubular and stretched vesicles (Fig. 4e), bearing rare microphenocrysts of acicular labradorite to andesine plagioclase (up to 200 mm) and Fe-rich olivine (~25 μm) within a glassy groundmass with rare microlites of plagioclase, clinopyroxene olivine, and Fe-Ti oxides. Some pumice fragments, which have coarse amoeboid and collapsed vesicles, have domains with glassy groundmass and domains with microcrystalline ones (Fig. 4e). Loose crystals of plagioclase, clinopyroxene, and olivine are also present. Lithic clasts include reddish to pinkish, oxidized pumices and rare fragments of granitoid rocks.

Major, minor, and trace elements glass geochemistry

Representative major, minor, and trace element glass chemistry from the BRH 1 to 5 tephra layers are provided in Table 1, whilst the full datasets are provided in the Supplementary Information.

The tephra layers analyzed (BRH1 to 5) display more than one compositional component, consistent with their variable textures and componentry; consequently, compositions range from basalts, through basaltic trachy-andesites and trachy-andesites to more evolved trachytes (Fig. 5a). Glasses are all characterized by high analytical totals suggesting a very minor amount of post-depositional alteration and/or reworking.

BRH1 to 5 volcanic glasses predominantly straddle the high-K calc-alkaline and Shoshonitic boundary, with the more evolved trachytic end-members residing more clearly within the shoshonitic field (Fig. 5b). The absence of negative anomalies at Nb and Ta in the mantle-normalized trace element profiles of the BRH1 to 5 volcanic glasses is clearly consistent with Antarctic alkaline regional volcanism within the West Antarctic Rift System (Panter 2021), and the absence of significant crustal involvement in magma genesis (Fig. 6). As is to be expected, overall levels of incompatible trace element enrichment are significantly greater in the trachytic end-member glasses of the tephra units relative to their more mafic components (Fig. 7). Light Rare Earth Elements (LREE) are enriched relative to the Heavy Rare Earth Elements (HREE), and the relative level of enrichment remains fairly constant spanning from the basalts through to the trachytes (La/Yb_N ~ 13–14). Trachytic end-member glasses display depletions in Ba, Sr, and Eu consistent with feldspar fractionation, with these anomalies absent in the more primitive (basaltic) glasses. Owing to the significant heterogeneity of the BRH tephra layers, we describe the chemical signature of dominant chemical clusters or components, and therefore rare outlying analyses are not described in detail.

BRH1 (*n = 18/24*), BRH2 (*n = 13/33*), and BRH5 (*n = 15/30*) tephra layers all contain a significant mafic glass component associated with the black glassy and fluidal particles, which display a relatively narrow compositional range within the basalt compositional field (44.5 to 46.0 wt% SiO_2, and 3.9 to 5.3 $Na_2O + K_2O$), with minor overlap into the basanite field (Fig. 5a). More noticeable compositional variability in these basalts is observed in other major oxides, for instance with 7.3–4.7 wt% MgO, 14–12 wt% FeOt, 12.1–9.7 wt% CaO, and 5.0–3.3 wt% TiO_2, where this variability is consistent between the basalts of all three layers (Fig. 5). Tephra layer BRH3 also contains dark glassy material entirely consistent with the basaltic glasses of the BRH1, 2, and 5 tephra layers; however, these compositions are not as well represented in the chemical analysis of the tephra (*n = 10/74*), which are dominated by a trachytic end-member (Fig. 5a).

The incompatible trace elements content of these basaltic glasses, predominantly those successfully analyzed from the BRH1 and BRH5 layers, reveal significant variability, for instance 128–236 ppm Zr, 15.3–28.0 ppm Y, and 2.6–4.7 ppm Th (Fig. 7). Ratios of High Field Strength Elements (HFSE) vs. Th in these basaltic glasses show some variability (e.g. Zr/Th = 46.3–54.3; Nb/Th = 14.2–15.5; Y/Th = 5.6–6.6). These basaltic glasses display high LREE relative to the HREE where $La/Yb_N = 13.0 \pm 0.9$ (1 s.d). Despite the overall variability within the basaltic glasses analyzed, they are chemically indistinguishable through the successive tephra layers, suggesting a common magmatic source.

BRH1 glasses, consistent with the observed componentry (see above), are chemically bimodal; in addition to the dominant dark glassy basaltic component already described, the tephra layer also contains a homogeneous secondary trachytic component ($SiO_2 = 65.2 \pm 0.1$ wt% and

Table 1 Representative major, minor, and trace elements glass data for the BRH1 to 5 tephra deposits investigated. *Bas*, basalt; *Bas Tra-And*, basaltic trachy-andesite; *Tra-And*, trachy-andesite; *Tra*, trachyte. Full geochemical data sets are available in the Supplementary material file

	BRH 1		BRH 2			BRH 3			BRH 4			BRH 5		
TAS class	Bas	Tra	Bas	Bas Tra-And	Tra-And	Basalt	Bas. Tra-And	Tra	Bas Tra-And	Tra-And	Tra	Bas	Tra	Tra
Norm. wt%														
SiO_2	45.52	65.11	45.27	55.28	61.09	45.28	54.70	66.67	54.45	57.63	64.13	45.17	64.85	66.77
TiO_2	4.83	0.50	4.64	2.03	0.99	3.95	2.21	0.35	1.97	1.69	0.84	4.11	0.46	0.40
Al_2O_3	14.31	15.87	14.90	15.15	15.08	14.70	14.39	15.54	15.43	14.94	14.73	14.92	15.85	15.33
FeOt	13.96	5.30	13.61	11.46	8.88	12.98	11.66	4.76	11.21	10.44	6.99	12.87	5.68	4.85
MnO	0.15	0.11	0.21	0.25	0.19	0.17	0.25	0.12	0.19	0.21	0.21	0.15	0.16	0.17
MgO	5.12	0.16	5.24	2.04	0.81	6.12	2.07	0.16	1.91	1.50	0.60	5.94	0.21	0.19
CaO	10.21	1.85	10.45	5.97	3.65	11.61	5.95	1.78	6.05	4.60	2.37	11.70	1.92	1.80
Na_2O	3.61	5.91	3.67	4.37	5.33	3.34	5.19	5.47	4.82	4.73	5.10	3.31	5.62	5.41
K_2O	1.26	4.98	1.20	2.56	3.55	1.21	2.71	4.91	2.90	3.56	4.66	1.12	4.99	4.85
P_2O_5	0.94	0.03	0.74	0.78	0.31	0.56	0.77	0.04	0.96	0.55	0.20	0.64	0.04	0.07
Cl	0.08	0.19	0.06	0.11	0.12	0.07	0.10	0.19	0.13	0.14	0.17	0.06	0.22	0.18
Ana. Total	99.16	99.54	99.19	99.62	99.04	98.36	99.69	99.13	98.75	98.19	99.51	98.69	99.02	99.75
Na_2O+K_2O	4.87	10.89	4.87	6.93	8.88	4.56	7.90	10.39	7.71	8.29	9.76	4.43	10.62	10.26
ppm														
Rb	32.0	167.8	19.6	-	115.5	26.4	74.4	154.9	83.1	94.7	139.2	26.9	160.2	157.9
Sr	643	142	561	-	408	660	612	148	454	437	218	625	135	157
Y	27.0	54.4	15.3	-	47.5	23.8	42.9	51.8	48.8	44.1	46.7	23.0	56.8	54.0
Zr	222	687	128	-	504	197	373	685	449	469	605	189	709	711
Nb	68	165	37	-	127	59	102	152	118	120	141	54	165	157
Ba	371	1097	231	-	1052	328	831	1117	843	922	977	301	1044	1188
La	40.6	101.8	23.0	-	85.1	35.2	73.1	96.8	82.3	77.5	88.7	32.1	103.9	100.6
Ce	84.8	197.9	48.1	-	169.4	75.0	150.7	190.1	169.1	157.4	176.3	67.6	202.4	193.5
Pr	9.6	20.5	5.5	-	18.7	8.5	16.8	19.7	18.7	17.0	18.4	7.9	21.3	20.3
Nd	41.5	77.5	23.3	-	71.9	36.2	68.9	74.4	75.9	69.4	69.2	33.6	83.3	73.3
Sm	9.0	14.6	4.7	-	13.8	7.6	12.8	13.6	15.0	13.3	13.0	7.3	15.0	14.4
Eu	2.9	2.9	1.6	-	3.8	2.6	4.3	2.7	4.4	3.9	2.9	2.3	3.0	2.7
Gd	7.4	11.3	4.4	-	11.4	6.6	10.9	10.9	12.6	10.8	10.7	6.4	12.0	11.5
Dy	5.9	10.5	3.5	-	9.6	5.2	9.1	10.3	10.5	9.4	9.3	5.0	11.7	11.0
Er	2.7	5.7	1.6	-	4.7	2.5	4.3	5.4	5.0	4.5	4.7	2.5	6.1	5.8
Yb	2.3	5.4	1.2	-	4.3	1.8	3.6	5.5	4.2	4.3	4.7	2.0	5.6	5.4
Lu	0.3	0.7	0.2	-	0.6	0.3	0.5	0.7	0.6	0.6	0.6	0.3	0.8	0.8
Hf	5.3	15.1	3.1	-	10.8	4.7	8.6	15.4	10.3	10.5	13.2	4.5	16.2	16.1
Ta	4.1	9.2	2.2	-	6.7	3.6	5.9	8.6	6.6	6.8	7.7	3.2	9.1	8.9

Table 1 (continued)

	BRH 1		BRH 2			BRH 3			BRH 4			BRH 5		
TAS class	Bas	Tra	Bas	Bas Tra-And	Tra-And	Basalt	Bas. Tra-And	Tra	Bas Tra-And	Tra-And	Tra	Bas	Tra	Tra
Pb	2.3	23.8	1.4	-	14.8	1.9	8.7	18.7	9.2	11.3	16.1	3.0	19.3	19.2
Th	4.4	21.0	2.6	-	14.6	3.9	10.8	20.8	12.2	13.0	17.2	3.7	22.0	22.1
U	1.4	5.0	0.7	-	3.4	1.2	2.5	4.4	2.9	3.1	4.1	1.3	5.0	4.6
Zr/Th	50.4	32.6	49.1	-	34.4	50.9	34.4	32.9	36.9	36.1	35.1	51.5	32.2	32.2
Nb/Th	15.4	7.8	14.3	-	8.7	15.2	9.4	7.3	9.7	9.2	8.2	14.7	7.5	7.1
Y/Th	6.1	2.6	5.9	-	3.2	6.1	4.0	2.5	4.0	3.4	2.7	6.3	2.6	2.4

$Na_2O + K_2O = 10.78 \pm 0.1$ wt%; *n = 5/23*). The incompatible trace element contents of these trachytic glasses (*n = 4*) are relatively homogeneous, for instance 676 ± 40 ppm Zr, 54 ± 4 ppm Y, and 21 ± 2 ppm Th, whilst these levels of enrichment far exceed those of the dominant basaltic end-member (Fig. 7). Ratios of HFSE vs. Th become significantly lower (Zr/Th = 33.0 ± 1.3; Nb/Th = 8.1 ± 0.5; Y/Th = 2.6 ± 0.1 [1 s.d]) than those of the basaltic component (Fig. 7). These evolved trachytic glasses display particularly strong negative Sr anomalies ($Sr/Pr_N = 0.09 \pm 0.003$), but also less pronounced anomalies in Ba and Eu (Fig. 6).

Overall, BRH2 glasses cover a wide compositional range, consistent with the mixed componentry (see the "Texture and components of tephra layers" section). As with BRH1, the basaltic glass forms a significant component (1) of BRH2. In addition, at least two other compositional components or clusters are observed in BRH2, which plot along an evolutionary trend that extends towards the highly evolved trachytes, similar to the overlying BRH1 tephra (~65 wt% SiO_2). BRH2 glass component 2 straddles the boundary between the basaltic trachy-andesite to trachy-andesite compositional fields with between 54.5 and 56.5 wt% SiO_2 and where $Na_2O + K_2O = 6.9$–8.4 wt% (Fig. 5a). BRH2 component 3 glasses are more variable and evolved than component 2 predominantly clustering at the boundary between the trachy-andesite and trachytic field, albeit with a small number of analyses extending towards the more evolved trachytic endmember of BRH1 (Fig. 5a).

Trace element analysis of BRH2 component 2 (basaltic trachy-andesite/trachy-andesite) glasses was unsuccessful due to the presence of microlites, but trace element analyses were acquired for glass component 3. The trachy-andesites through to trachytes are equally heterogeneous at the trace element level, with 388–720 ppm Zr and 10.0–21.9 ppm Th. The glasses show depletions in Sr ($Sr/Pr_N = 0.30 \pm 0.1$ [1 s.d]) and Eu; however, these are not as pronounced as those observed in the more evolved trachytes of BRH1 (Fig. 6). HFSE ratios to Th in these glasses remain constant despite the variability in absolute concentrations (Zr/Th 33.6 ± 1.6; Nb/Th = 8.4 ± 0.9; Y/Th = 3.1 ± 0.2 [1 s.d]). The Zr/Th and Nb/Th ratios are broadly consistent with the more evolved (trachytic) glasses of the overlying BRH1, but again are significantly lower than those of the basaltic glasses in this tephra (and BRH1; Fig. 7).

In addition to a basaltic component, the BRH3 tephra has a minor population of intermediate glasses which straddle the basaltic trachy-andesite to trachy-andesite compositional fields, similar to component 2 of the overlying tephra BRH2 (Fig. 5a). A significant component of BRH3 analyses (*n = 51/73*) lies firmly in the trachytic compositional field, with 62.1–67.2 wt% SiO_2 and 8.8–10.6 wt% $Na_2O + K_2O$ and relate to the pumiceous material within this tephra layer. Within these variable trachytic compositions, a dominant

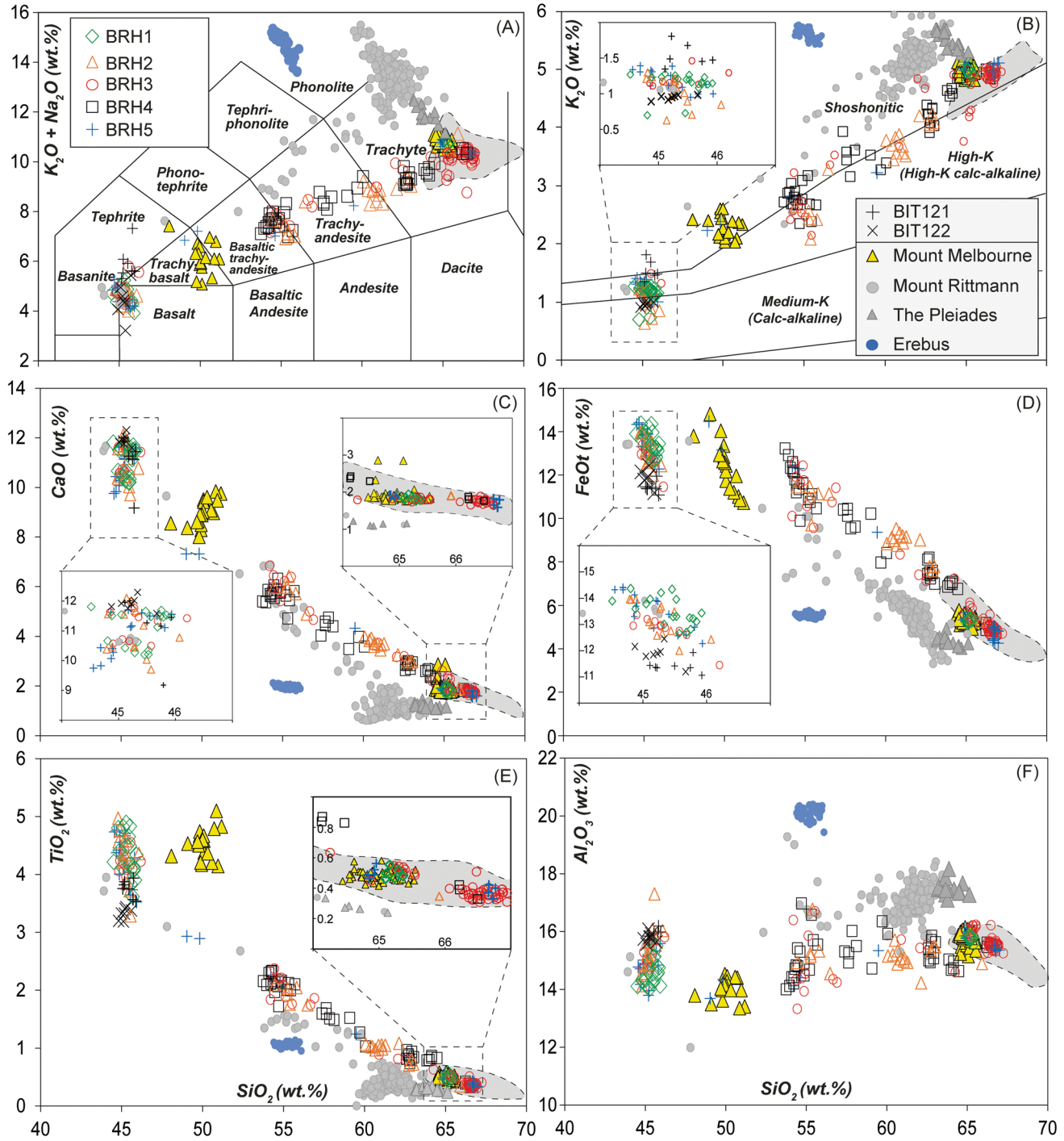

Fig. 5 Bivariate major elements plots depicting the significant volcanic glass heterogeneity of the BRH1 to 5 tephra deposits which range from basalts through to trachytes. (**A**) Total alkalis vs. silica classification diagram (TAS) following LeBas et al. (1986); (**B**) K_2O vs. SiO_2 following Peccerillo and Taylor (1976). The trachytic glasses of the BRH 1 to 5 tephra layers plot along the same evolution trend as those previously analyzed from Mount Melbourne (Del Carlo et al. 2022), and are offset from glasses erupted at nearby volcanic centres, such as Mount Rittmann (Di Roberto et al. 2019), the Pleiades (Lee et al. 2019), and Mount Erebus (Harpel et al. 2008). Black dashed line encircling the grey compositional field represents the TR17-08 tephra from Edisto Inlet and the black symbols indicate tephras from Brimstone Peak (+BIT121, ×BIT122; Dunbar 2003)

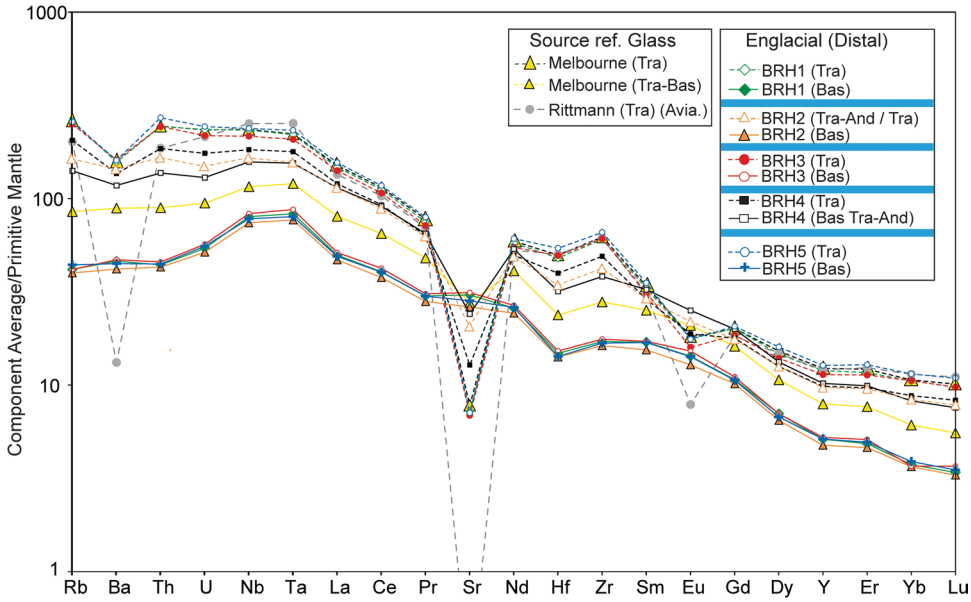

Fig. 6 Primitive mantle normalized (McDonough and Sun 1995) trace elements concentrations of volcanic glass (component averages) for the BRH1 to 5 tephra layers. The data presented clearly illustrate a chemical link between the trachytic end-member glasses of the BRH tephra layers and those found at the summit of Mount Melbourne (Del Carlo et al. 2022). Bas—basalt; Tra-Bas—trachy-basalt; Bas Tra-And—basaltic trachy-andesite; Tra-And—trachy-andesite; Tra—trachyte

cluster of shoshonitic glasses is clearly recognized at ~ 66 wt% SiO_2, and ~ 4.9 K_2O (Fig. 5b), where Na_2O is > K_2O ($K_2O/Na_2O = 0.9$). These most evolved trachytes ($n = 16$) are extremely enriched in incompatible trace elements, for instance 613–728 ppm Zr and 18.3–22.1 ppm Th. HFSE ratios vs. Th in these trachytic glasses remain constant where Zr/Th = 33.0 ± 0.8, Nb/Th = 7.5 ± 0.3, and Y/Th = 2.5 ± 0.1 (Fig. 7). They also display depletions in Ba, Sr ($Sr/Pr_N = 0.10 \pm 0.01$), and Eu (Fig. 6).

The glass compositions of BRH4 are heterogeneous, largely bimodal, with some glasses extending between the two dominant end-members. The least evolved glass component plots in the basaltic trachy-andesite compositional field ($SiO_2 = 53.8–55.7$ wt% SiO_2, $Na_2O + K_2O = 7.0–8.3$), whilst straddling the boundary with trachy-andesites (Fig. 5a). The more evolved end-member is characterized by slightly more variable trachytic glass compositions with 62.6–66.5 wt% SiO_2 and 9.1–10.5 wt% $Na_2O + K_2O$ (Fig. 5a) and these relate to the pumice component of the deposit. The basaltic trachy-andesitic glasses ($n = 5$) have some incompatible trace element variability, for instance 400–449 ppm Zr and 11.3–12.3 ppm Th (Fig. 7). The HFSE ratios in

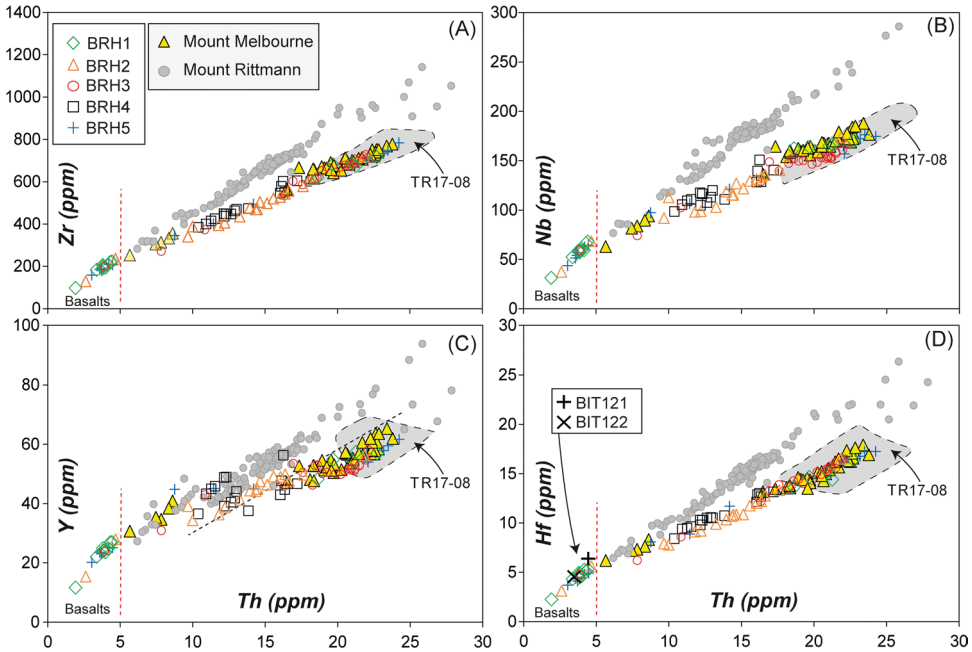

Fig. 7 Bivariate trace elements plots, specifically (**A**) Th vs Zr, (**B**) Th vs Nb, (**C**) Th vs Y, and (**D**) Th vs Hf, depicting the significant heterogeneity of the BRH1 to 5 tephra layers consistent with their major elements variability ranging from basalts to trachytes. The plots illustrate the significant chemical overlap of these successive tephra deposits, which clearly lie upon an evolutionary trend indistinguishable from the products of Mount Melbourne (mainly trachytic), and offset from those of the nearby Mount Rittmann (after Del Carlo et al. 2022). The grey compositional field is for Edisto Inlet tephra TR17-08, whereas the black symbols indicate the average composition of Brimstone Peak tephras (+BIT121,×BIT122; Dunbar 2003)

these glasses are constant (36.7 ± 0.2 Zr/Th, 9.6 ± 0.1 Nb/Th, and 4.0 ± 0.02 Y/Th [1 s.d]), whilst they show a small anomaly in Sr ($Sr/Pr_N = 0.4 \pm 0.1$ [1 s.d]). The trachytic end-member glasses ($n = 5$) are more enriched in incompatible elements than the basaltic trachy-andesites (Fig. 7), and show considerable variability, for instance 472–604 ppm Zr and 13.8–17.2 ppm Th. These trachytic glasses display constant HFSE ratios (e.g. 34.7 ± 1.0 Zr/Th, 8.2 ± 0.4 Nb/Th, and 2.8 ± 0.3 Y/Th), but are slightly lower than those of the basaltic trachy-andesites. The trachytic glasses display a greater depletion in Sr ($Sr/Pr_N = 0.3 \pm 0.1$), along with additional depletions in Ba and Eu in contrast to the basaltic trachy-andesites (Fig. 6). However, the removal of Sr from the melt composition of BRH4 is not as significant as for some of the more evolved trachytic glasses observed in the overlying tephra deposits (e.g. BRH1, BRH3; Fig. 6).

Compositionally, the BRH5 tephra layer is largely bimodal, with some very minor evidence of intermediate glass compositions spanning an evolutionary trend between the two end-members, which are characterized by basaltic and trachytic glass populations (Fig. 5a). The basaltic component is entirely consistent with those observed and described (above) from the BRH1, BRH2, and BRH3 tephra layers (Figs. 5, 6, and 7). Whilst the trachytic end-member glasses are variable, they remain consistent with both dominant trachytic components of BRH1 and BRH3, where SiO_2 contents of ~ 64.9 wt% and ~ 66.8 wt% respectively are observed (Fig. 5a). The incompatible trace element contents of the BRH5 trachytic endmember ($n = 5$) glasses are homogeneous with 737 ± 30 ppm Zr and 23 ± 1 ppm Th. The levels of enrichment in some of these trachytic glasses extend to the highest observed throughout this englacial succession (Fig. 7). Furthermore, strong depletions in Ba, Sr ($Sr/Pr_N = 0.09 \pm 0.01$ [1 s.d]), and Eu are observed in these glasses (Fig. 6). HFSE ratios to Th are constant (32.0 ± 0.3 Zr/Th, 7.3 ± 0.2 Nb/Th, 2.5 ± 0.1 Y/Th [1 s.d]) and are entirely consistent with the most evolved trachytic products seen in the BRH1 and BRH3 layers.

Discussion

Volcanic source and proximal-distal correlation

Major and trace elements glass composition data show a strong geochemical affinity between the BRH tephra and the products of MMVF, plotting along the same evolutionary trend. This compositional similarity and the proximity of these tephra layers to MMVF suggest they were erupted from its vents (Figs. 5 and 7). BRH major and trace elements compositions plot along the evolutionary trend defined by volcanic glasses of MMVF (Figs. 5 and 7), which is distinct from other volcanoes in the region. However, there is no direct match between the composition of BRH tephra and that of late Pleistocene to Holocene tephra layers exposed in the summit of Mount Melbourne, recently characterized compositionally by Del Carlo et al. (2022) are characterized by generally higher alkali and lower silica contents. In addition, Mount Melbourne summit proximal deposits lack the basaltic end-member compositions which instead are common in the BRH products except for the BRH4 tephra. Thus, the BRH tephra layers are likely to result from eruptions at separate vent areas, possibly from parasitic cones located on the flank of the volcano or at the periphery of the Mount Melbourne volcanic complex. On the eastern flank of Mount Melbourne, a few kilometres NNW of Edmonson Point ropey basaltic lava and a hawaiite scoria cone are observed, known respectively as the ROL and SCC outcrops of Giordano et al. (2012). These sources are close enough and their deposits are compatible with the characteristics and the eruption styles of BRH tephra. Also, the parasitic cones NNW of the summit of Mount Melbourne, which have trachytic compositions, and possibly scoria cones on the south side of Random Hills further to the north (Smellie et al. 2023) could be considered possible sources. Unfortunately, these only the eruptive centres close to Edmonson Point are dated, and not precisely. They are only constrained to the last 90 ka (Giordano et al. 2012; Smellie et al. 2023), hampering direct correlations.

We also compared the composition of the BRH tephra with visible tephra and cryptotephra layers identified in the marine record of the Ross Sea and in the glacial records of northern Victoria Land.

Interestingly, the composition of trachytic particle population in BRH3 and BRH5, the deepest and middle tephra respectively among those studied, correlates very well with the composition of three cryptotephra recently identified in the TR17-08 piston sediment core recovered in Edisto Inlet, near Cape Hallett, more than 280 km from Melbourne volcano (Di Roberto et al. 2023; Fig. 1). These cryptotephra layers, namely TR17-08-512, -518, and -524, have a trachytic composition (Figs. 5 and 7) and comprise colourless to light-green glass shards and pumice fragments, characterized by pristine textures among blocky, y-shaped, and bubble wall morphology whilst preserving fragile glass tips. Within core TR17-08, tephra age was defined using radiocarbon dating of carbonate material, intercalated with tephra, and was constrained between 1615 cal. years BP and 1677 cal. years BP, i.e. between the third and fourth century AD (Di Roberto et al. 2023). These TR17-08 tephra layers have been interpreted as produced by a series of explosive eruptions from the Mount Melbourne volcanic complex that occurred closely spaced in time, with a maximum interval of c. 60 years between events (Di Roberto et al. 2023).

The geochemical correlation defined between BRH proximal tephra and distal marine tephra allows the former to be

indirectly dated and consequently defines the onset (and an overall age) of this eruptive period of Mount Melbourne between the third and fourth century AD. The results confirm that Mount Melbourne has been very active in historical times, with more explosive eruptive events than previously thought.

For the sake of completeness, it should be said that some differences exist between the BRH and TR17-08 cryptotephra. The most notable regards the lack of basaltic glass populations in TR17-08 samples. The lower viscosity of the denser melts typically results in less fragmentation and lower plume heights of the basaltic phases that limit the tephra dispersal. This is consistent with the significantly larger grain size characterizing the basaltic ash (and lapilli) in the studied tephra. The higher abundance of fine ash in the trachytic end-member testifies to more efficient magmatic fragmentation, and these finer particles are transported further, especially those associated with the intense phases of the eruption with high plumes. Moreover, whilst three cryptotephra have been identified within the TR17-08 marine core, only two tephra with similar trachytic compositions were recovered at the BRH site. Another layer may be preserved deeper in the ice sequence, below the BRH5 tephra, or was eroded at the BRH site.

Furthermore, we explored correlations with tephra from the ice core records of Styx Glacier (SG), Talos Dome (TD), and the blue ice areas of Brimstone Peak (75.888S 158.55E; BIT Dunbar et al. 2003), located at ca. 35 km, 230 km, and 250 km ESE from the sampling site, respectively. Unfortunately, most of the geochemical data for SG, TD, and BIT tephra layers comprise only major element glass composition for which the accuracy is not clear, and lack trace element glass data, which hamper reliable correlations with the BRH tephra layers.

In spite of this, we found a major similarity between the trachytic compositions of BRH4 tephra and the TD85 tephra layer in the Talos Dome record dated at c. 670 yrs BP (1280 CE; Narcisi et al. 2012; Severi et al. 2012), but it is not a viable correlation based on other tephrostratigraphic evidence. In the Talos Dome record, the TD87a tephra correlates to the 1254 CE eruption of Mount Rittmann, and is located c. 2 m below the TD85 (Severi et al. 2012). Given that the 1254 CE tephra is ubiquitous in the marine and glacial records of the Ross Sea and northern Victoria Land, a significant and widespread tephra marker (Di Roberto et al. 2019 and references therein), and it is not between BRH4 and BRH5 in the proximal exposure, we conclude that BRH4 does not correlate to TD85.

A tephrostratigraphy similar to that of Talos Dome has been developed for the Styx glacier ice core (which is the ice record closer to the studied BRH site), where the 1254 CE tephra was detected at a depth of 99.18 m and is only overlaid by another tephra at 97.01 m (Han et al. 2015), instead of five ash layers.

Vice versa, our data confirm that TD85 likely derives from Mount Melbourne volcanic activity, as previously suggested by Narcisi et al. (2012), based on the major element data. If this correlation would be verified using trace element glass compositions, it would affirm that Mount Melbourne was active in even more recent times, less than 700 years ago. This further shows that incomplete geochemical databases strongly limit correlation efficacy, and high-quality geochemical data are necessary to make reliable correlations.

A general geochemical affinity also exists between BRH1, BRH2, and BRH5 tephra and the composition of BIT volcanic ash (Dunbar 2003). In detail, there is a strong similarity in major element compositions between the BRH1, BRH2, and BRH5 basalt to basanite glass population and the BIT121 and BIT122 ash layers (Fig. 5). Trace element compositions of BIT are not entirely determined, and the same similarity can be only documented in the Th vs Hf plot (Fig. 7d). BIT121 and BIT122 layers are respectively a thick dark brown unit made of clear, aphyric, and dense blocky shards (BIT121) and a grey diffuse layer with clear to olive green glass, blocky shards with spherical vesicles, plus droplets and glass hairs. In particular, the latter has strikingly similar textural characteristics to the BRH tephra. Unfortunately, BIT volcanic ash layers lack chronological and appropriate trace element information, and thus cannot be definitively correlated with BRH.

Eruption dynamics

Componentry, textures, and geochemical fingerprints of the studied tephra indicate that these layers have been emplaced as primary fallout deposits. As mentioned above, the external morphology of particles that preserves pristine features like fragile glass tips, Pele's hair, or spiny glass edges (Figs. 3 and 4) and glass coatings around magmatic crystals indicate minor or no aeolian remobilization, re-sedimentation, or other transport after deposition from the volcanic plume.

The volcanic glass composition of each sample, which is strongly bimodal with other analyses along geochemical trends, always lies on the same evolutionary compositional lineage indicating the same volcanic source (see Del Carlo et al. 2018). The proximity of these decimetre-thick units to the MMVF, and their shared geochemical affinity, is consistently being from Mt. Melbourne or other vents around the summit. The absence of large amounts of detrital material, including glass particles from other volcanic sources, is evident and indicates negligible reworking, re-sedimentation, and redistribution of pyroclastic products.

Glass particles forming the studied deposits comprise a variety of fragments differing in external shape, vesicularity, mineral content, and composition. Internal and external textural inhomogeneity is widely documented in the products of explosive eruptions from many volcanoes and has been ascribed to changes in the ascent and/or flow conditions during the eruption and to diverse mechanisms of particle fragmentation (i.e. hydromagmatic vs magmatic), transport, and the eruptive environment (see, e.g. D'Oriano et al. 2022 and references therein).

The almost ubiquitous presence of fluidal fragments including Pele's hair and tears (i.e. fibres and droplets of volcanic glass; Figs. 3 and 4) indicates specific eruptive dynamics and magma properties typical of magmatic eruptions. Fluidal fragments and Pele's hairs and tears formed by the stretching, deformation, and final magma breakup of very hot, low-viscosity magma due to interfacial shear between gas and melt (see Lin and Reitz 1998; Eggers and Villermaux 2008). Pele's hairs and tears form during subaerial Hawaiian-style eruptions fed by low-viscosity basaltic melts (Heiken and Wohletz 1985) and are also common, but minor, in basaltic eruptions occurring in sub-aqueous environments (Clague et al. 2000, 2003). Similarly, the presence of abundant moderately to highly vesicular basaltic particles with cuspate to spongy external surfaces is indicative of pure magmatic fragmentation of gas-rich melts dominated by exsolution and expansion of magmatic gas, for example in a Strombolian column.

More equant and blocky particles have irregular contours, are bounded by sharp planar edges, and are made of dense to poorly vesicular glass, bearing features like stepped surfaces and quenching cracks, as well as hackle lines and surface pitting (Fig. 4i–l), which are distinctive of phreatomagmatic fragmentation (Fisher and Schmincke 1984; Heiken and Wohletz 1985; Morrissey et al. 2000; Dürig et al. 2012; Zimanowski et al. 2015; Ross et al. 2022). Stepped features are a consequence of the extreme and intensive brittle fracturing of the melt (Zimanowski et al. 2015). The water, in direct contact with the hot melt, expands and exerts a massive hydraulic pressure onto the melt itself, which behaves in a brittle way, so that cracks are occurring, driven by the applied stress; still, liquid water is pushed into the propagating crack, thus increasing the interface area between magma and water and therefore increasing the heat flux from magma to water, generating an accelerating thermohydraulic feedback loop (Dürig and Zimanowski 2012; Dürig et al. 2012). Hackle lines indicate the direction of propagation of a crack and, since these can form during slow or fast cracking, are not strictly diagnostic of melt-water interaction, although some fragmentation experiments with water produce increased proportions of particles with hackle lines relative to others without water (Ross et al. 2022). Quenching cracks form immediately after fragmentation due to the sudden quenching and consequent contraction of still-hot particles due to the fast contact with liquid water (Zimanowski et al. 2015). Pitted surfaces indicate incipient alteration resulting from the interaction of glass with hydrothermal fluids (or excess water) in the eruptive column (Zimanowski et al. 2015; Ross et al. 2022).

The simultaneous presence of particle morphologies with features indicative of magmatic and hydromagmatic fragmentation in BRH tephra layers is evidence that various degrees of magma-water interaction occurred during the forming eruptions. For example, texturally mixed deposits could derive from the transformation of an initially subglacial, hydromagmatic eruption fuelled by the interaction between magma and meltwater, into a relatively dry magmatic subaerial Hawaiian- to Strombolian-style eruption, once the water source was exhausted and drained or the magma no longer came into contact with the meltwater (vent completely subaerial). As mentioned above, the major and trace element glass compositions of the heterogeneous BRH1 to 5 tephra deposits are largely overlapping, and clearly reside on the same evolutionary trends indicating they all likely derive from the same magmatic system. The overall chemical variability (ranging from basalts through to trachytes) and in particular the observed clustering of the erupted volcanic glass compositions along the overall evolutionary trend might indicate that the successive eruptions were fed by a complex and vertically extensive magma storage region beneath the source volcano (Cashman et al. 2017; Giordano and Caricchi 2022). This is quite common as reported for several eruptions (see Shane and Hoverd 2002; Shane et al. 2007, 2008).

Interestingly, apart from BRH4, all the remaining BRH tephra deposits comprise a basaltic glass component, and the interaction of the mafic melt with more evolved trachy-andesitic to trachytic magma pockets, or mush, is the likely trigger of these eruptions. In this regard, it should be highlighted that at least during some of the eruptive phases emplacing BRH tephra, a trachytic magma was fragmented efficiently enough to disperse the ash several hundred kilometres away. This is possible only during high-intensity eruptions able to produce eruptive columns of significant heights, as hypothesized by Di Roberto et al. (2023).

Conclusions

BRH1 to 5 tephra are primary fallout layers derived from five explosive eruptions that occurred in a short time from within the Mount Melbourne Volcanic Field. The nature and texture of particles forming the tephra layers indicate that the eruptions were mostly Hawaiian to Strombolian in style

and characterized by magmatic and possibly hydromagmatic fragmentation occurring over the time of the eruption. The distal dispersal of trachytic ashes to some hundreds of kilometres from the source (c. 280 km) also demonstrates that the BRH eruptions were at some time characterized by a strong explosivity and very efficient magma fragmentation, and possibly produced several kilometre-high eruptive columns.

The magma compositions feeding the eruptions range from basalts to trachytes and the clustering of the erupted product compositions indicates that the eruptions were fed by a complex and vertically extensive magma system region beneath the source volcano with the mafic melt remobilizing more evolved trachy-andesitic to trachytic magma pockets.

Although the geochemical data confirm that the volcanic source of BRH1 to 5 tephra is the Mount Melbourne volcano, there is no direct match between the composition of tephra studied here and Pleistocene to Holocene tephra layers exposed in the summit part of Mount Melbourne characterized by Del Carlo et al. (2022; MEL samples). This potentially indicates that BRH tephra originated from vents located away from the summit area.

The geochemical correlations assessed between the BRH tephra deposits and three marine cryptotephra intercalated in sediments of the Edisto Inlet (TR17-08-512, -518, and -524), which were dated by the radiocarbon method between 1615 cal. years BP and 1677 cal. years BP, allowed to indirectly constrain the ages of BRH eruptions between the third and fourth century CE. This finding improves our knowledge of the eruptive history of Mount Melbourne volcano, which has produced at least five eruptions during historical time, increasing the awareness of potential hazards to the several permanent scientific bases close to Mount Melbourne.

Moreover, the attribution of a numerical age to the BRH tephra elevates them to new regional isochron markers that will possibly enhance the correlation and synchronization of climatic records of the northern Victoria Land and Ross Sea areas.

This study demonstrates the robustness of the tephrochronological method in terms of correlation and dating of glacial, terrestrial, and marine records, if carried out with a modern approach and up-to-date techniques. The need for high-quality textural, mineralogical, and compositional data (major and trace element glass compositions) on tephra is even more evident for Antarctica, where outcrops are scarce. Only with an exhaustive fingerprinting of tephra layers is possible to establish effective correlations between different records enhancing synchronization and correlations for palaeoenvironmental and palaeoclimatic reconstructions.

Supplementary information The online version contains supplementary material available at https://doi.org/10.1007/s00445-023-01651-2.

Acknowledgements We acknowledge ENEA for providing field logistics at Mario Zucchelli Station. We are grateful to the pilots J. Henery and B. McElhinney for the helicopter surveys and the Italian alpine guides M. Bussani and D. De Podestà for sampling the ice cliff and their assistance in the fieldwork. Dr C. Manning is also acknowledged for her assistance with the LA-ICP-MS analysis. We also thank the editors J.L. Smellie and G. Giordano, and an anonymous reviewer for their revisions that greatly improved the paper. This paper is dedicated in memory of Antonio De Sio (Tony), an Antarctic friend of ours.

Author contribution P.D.C., A.C., G.G., and G.L. carried out the fieldwork and sampling on the flanks of Mt. Melbourne. P.D.C. and A.D.R. conceived the research. P.D.C., A.D.R., G.R., and B.S. carried out the textural analysis of the volcanic glass and the petrographic analysis, and interpreted geochemical and petrological data. P.G.A. and V.C.S. carried out the major and trace element geochemical analyses, respectively. All authors contributed to data interpretation, the writing of the manuscript, and the preparation of the figures.

Funding Open access funding provided by Istituto Nazionale di Geofisica e Vulcanologia within the CRUI-CARE Agreement. This work was funded by the Projects: ICE-VOLC (multiparametrIC Experiment at Antarctica VOLCanoes: data from volcano and cryosphere-ocean-atmosphere dynamics, www.icevolc-project.com/; PNRA 14_00011), TRACERS (TephRochronology and mArker events for the CorrElation of natural archives in the Ross Sea, Antarctica; PNRA2016—Linea A3/00055), and CHIMERA (CryptotepHra In Marine sEquences of the Ross Sea, Antarctica: implications and potential applications; PNRA18_00158-A). We acknowledge PNRA, the Italian Programma Nazionale di Ricerche in Antartide, for funding the projects. This paper is sponsored by the SCAR Expert Group, *AntVolc*.

Open Access This article is licensed under a Creative Commons Attribution 4.0 International License, which permits use, sharing, adaptation, distribution and reproduction in any medium or format, as long as you give appropriate credit to the original author(s) and the source, provide a link to the Creative Commons licence, and indicate if changes were made. The images or other third party material in this article are included in the article's Creative Commons licence, unless indicated otherwise in a credit line to the material. If material is not included in the article's Creative Commons licence and your intended use is not permitted by statutory regulation or exceeds the permitted use, you will need to obtain permission directly from the copyright holder. To view a copy of this licence, visit http://creativecommons.org/licenses/by/4.0/.

References

Adamson RG, Cavaney RJ (1967) Volcanic debris-layers near Mount Melbourne, Northern Victoria Land, Antarctica. New Zeal J Geol Geophys 10:418–421. https://doi.org/10.1080/00288306.1967.10426745

Armienti P, Civetta L, Innocenti F, Manetti P, Tripodo S, Villari L, Vita G (1991) New petrological and geochemical data on Mt. Melbourne Volcanic Field, Northern Victoria Land, Antarctica. (II Italian Antarctic Expedition). Mem Soc Geol It 46:397–424

Cashman KV, Sparks RSJ, Blundy JD (2017) Vertically extensive and unstable magmatic systems: a unified view of igneous processes. Science 355:eaag3055-11. https://doi.org/10.1126/science.aag3055

Clague DA, Moore JG, Reynolds JR (2000) Formation of submarine flat-topped volcanic cones in Hawai'i. Bull Volcanol 62:214–233. https://doi.org/10.1007/s004450000088

Clague DA, Batiza R, Head JW, Davis AS (2003) Pyroclastic and hydroclastic deposits on Loihi Seamount, Hawaii. Explosive Subaqueous Volcanism. AGU Geophys. Monogr 140:73–95. https://doi.org/10.1029/140GM05

Curzio P, Folco L, Ada Laurenzi M et al (2008) A tephra chronostratigraphic framework for the Frontier Mountain blue-ice field (northern Victoria Land, Antarctica). Quat Sci Rev 27:602–620. https://doi.org/10.1016/j.quascirev.2007.11.017

D'Oriano C, Del Carlo P, Andronico D, Cioni R, Gabellini P, Cristaldi A, Pompilio M (2022) Syn-eruptive processes during the January–February 2019 ash-rich emissions cycle at Mt. Etna (Italy): implications for petrological monitoring of volcanic ash. Front Earth Sci 10:824872. https://doi.org/10.3389/feart.2022.824872

Del Carlo P, Di Roberto A, Di Vincenzo G, Bertagnini A, Landi P, Pompilio M, Colizza E, Giordano G (2015) Late Pleistocene-Holocene volcanic activity in northern Victoria Land recorded in Ross Sea (Antarctica) marine sediments. Bull Volcanol 77:36. https://doi.org/10.1007/s00445-015-0924-0

Del Carlo P, Di Roberto A, D'Orazio M, Petrelli M, Angioletti A, Zanchetta G, Maggi V, Daga R, Nazzari M, Rocchi S (2018) Late Glacial-Holocene tephra from southern Patagonia and Tierra del Fuego (Argentina, Chile): a complete textural and geochemical fingerprinting for distal correlations in the Southern Hemisphere. Quatern Sci Rev 195:153–170. https://doi.org/10.1016/j.quascirev.2018.07.028

Del Carlo P, Di Roberto A, Di Vincenzo G, Re G, Albert PG, Nazzari M, Smith VC, Cannata A (2022) Tephrostratigraphy of proximal pyroclastic sequences at Mount Melbourne (northern Victoria Land, Antarctica): insights into the volcanic activity since the last glacial period. J Volcanol Geotherm Res 422:107457. https://doi.org/10.1016/j.jvolgeores.2021.107457

Di Roberto A, Colizza E, Del Carlo P, Petrelli M, Finocchiaro F, Kuhn G (2019) First marine cryptotephra in Antarctica found in sediments of the western Ross Sea correlates with englacial tephras and climate records. Sci Rep 9:10628. https://doi.org/10.1038/s41598-019-47188-3

Di Roberto A, Albert PG, Colizza E, Del Carlo P, Di Vincenzo G, Gallerani A, Giglio F, Kuhn G, Macrì P, Manning CJ, Melis R, Miserocchi S, Scateni B, Smith VC, Torricella F, Winkler A (2020) Evidence for a large-magnitude Holocene eruption of Mount Rittmann (Antarctica): a volcanological reconstruction using the marine tephra record. Quat Sci Rev 250:106629. https://doi.org/10.1016/j.quascirev.2020.106629

Di Roberto A, Scateni B, Di Vincenzo G, Petrelli M, Fisauli G, Barker SJ, Del Carlo P, Colleoni F, Kulhanek DK, McKay R, De Santis L (2021) Tephrochronology and provenance of an Early Pleistocene (Calabrian) tephra from IODP Expedition 374 Site U1524, Ross Sea (Antarctica). Geochem Geophys Geosystems 22:e2021GC009739. https://doi.org/10.1029/2021GC009739

Di Roberto A, Del Carlo P, Pompilio M (2021b) Chapter 6.1 Marine record of Antarctic volcanism from drill cores. Geol Soc London Mem 55:631 LP – 647. https://doi.org/10.1144/M55-2018-49

Di Roberto A, Re G, Scateni B, Petrelli M, Tesi T, Capotondi L, Morigi C, Galli G, Colizza E, Melis R, Torricella F, Giordano P, Giglio F, Gallerani A, Gariboldi K (2023) Cryptotephras in the marine sediment record of the Edisto Inlet, Ross Sea: implications for the volcanology and tephrochronology of northern Victoria Land, Antarctica. Quat Sci Adv 100079. https://doi.org/10.1016/j.qsa.2023.100079

Dunbar NW, Zielinski GA, Voisins DT (2003) Tephra layers in the Siple Dome and Taylor Dome ice cores, Antarctica: sources and correlations. J Geophys Res Solid Earth 108:2374. https://doi.org/10.1029/2002JB002056

Dunbar N (2003) Blue Ice Tephra II - Brimstone Peak. U.S. Antarctic Program (USAP) Data Center. https://doi.org/10.7265/N5MG7MDK

Dürig T, Zimanowski B (2012) "Breaking news" on the formation of volcanic ash: fracture dynamics in silicate glass. Earth Planet Sci Lett 335–336:1–8. https://doi.org/10.1016/j.epsl.2012.05.001

Dürig T, Mele D, Dellino P, Zimanowski B (2012) Comparative analyses of glass fragments from brittle fracture experiments and volcanic ash particles. Bull Volcanol 74:691–704. https://doi.org/10.1007/s00445-011-0562-0

Eggers J, Villermaux E (2008) Physics of liquid jets. Reports Prog Phys 71:36601. https://doi.org/10.1088/0034-4885/71/3/036601

Fisher RV, Schmincke J-U (1984) Pyroclastic rocks. Springer-Verlag, Berlin. https://doi.org/10.1007/978-3-642-74864-6

Gambino S, Armienti P, Cannata A, Del Carlo P, Giudice G, Giuffrida G, Liuzzo M, Pompilio M (2021) Chapter 7.3 Mount Melbourne and Mount Rittmann. Geol Soc London, Mem 55:M55–2018–43. https://doi.org/10.1144/M55-2018-43

Geyer A (2021) Chapter 1.4 Antarctic volcanism: active volcanism overview. Geol Soc London, Mem 55:M55–2020–12. https://doi.org/10.1144/M55-2020-12

Giordano G, Caricchi L (2022) Determining the state of activity of transcrustal magmatic systems and their volcanoes. Annu Rev Earth Planet Sci 50(2022):231–259. https://doi.org/10.1146/annurev-earth-032320-084733

Giordano G, Lucci F, Phillips D, Cozzupoli D, Runci V (2012) Stratigraphy, geochronology and evolution of the Mt. Melbourne volcanic field (North Victoria Land, Antarctica). Bull Volcanol 74:1985–2005. https://doi.org/10.1007/s00445-012-0643-8

Han Y, Jun SJ, Miyahara M, Lee H, Ahn J, Chung JW, Hur SD, Hong SB (2015) Shallow ice-core drilling on Styx glacier, northern Victoria Land, Antarctica in the 2014–2015 summer TT. J Geol Soc Korea 51(3):343–355. https://doi.org/10.14770/jgsk.2015.51.3.343

Harpel CJ, Kyle PR, Dunbar NW (2008) Englacial tephrostratigraphy of Erebus volcano, Antarctica. J Volcanol Geotherm Res 177:549–568. https://doi.org/10.1016/j.jvolgeores.2008.06.001

Heiken G, Wohletz K (1985) Volcanic ash. University of California Press, Berkeley

Hillenbrand C, Moreton SG, Caburlotto A, Pudsey CJ, Lucchi RG, Smellie JL, Benetti S, Grobe H, Hunt JB, Larter RD (2008) Volcanic time-markers for Marine Isotopic Stages 6 and 5 in Southern Ocean sediments and Antarctic ice cores: implications for tephra correlations between palaeoclimatic records. Quatern Sci Rev 27:518–540. https://doi.org/10.1016/j.quascirev.2007.11.009

Iverson NA, Kyle PR, Dunbar NW, McIntosh WC, Pearce NJG (2014) Eruptive history and magmatic stability of Erebus volcano, Antarctica: insights from englacial tephra. Geochem Geophys Geosystems 15:4180–4202. https://doi.org/10.1002/2014GC005435

Iverson NA, Kalteyer D, Dunbar NW, Kurbatov A, Yates M (2017) Advancements and best practices for analysis and correlation of tephra and cryptotephra in ice. Quat Geochronol 40:45–55. https://doi.org/10.1016/j.quageo.2016.09.008

Jochum KP, Pfänder J, Woodhead JD, Willbold M, Stoll B, Herwig K, Amini M, Abouchami W, Hofmann AW (2005) MPI-DING glasses: new geological reference materials for in situ Pb isotope analysis. Geochem Geophys Geosystems 6(10). https://doi.org/10.1029/2005GC000995

Jochum KP, Stoll B, Herwig K, Willbold M, Hofmann AW, Amini M, Aarburg S, Abouchami W, Hellebrand E, Mocek B, Raczek I, Stracke A, Alard O, Bouman C, Becker S, Dücking M, Brätz H, Klemd R, de Bruin D, Canil D, Cornell D, de Hoog C, Dalpé C, Danyushevsky L, Eisenhauer A, Gao Y, Snow JE, Groschopf N, Günther D, Latkoczy C, Guillong M, Hauri E, Höfer HE, Lahaye

Y, Horz K, Jacob DE, Kasemann SA, Kent AJR, Ludwig T, Zack T, Mason PRD, Meixner A, Rosner M, Misawa K, Nash BP, Pfänder J, Premo WR, Sun WD, Tiepolo M, Vannucci R, Vennemann T, Wayne D, Woodhead JD (2006) MPI-DING reference glasses for in situ microanalysis: new reference values for element concentrations and isotope ratios. Geochem Geophys Geosystems 7(2). https://doi.org/10.1029/2005GC001060

Kim D, Prior DJ, Han Y, Qi C, Han H, Ju HT (2020) Microstructures and fabric transitions of natural ice from the Styx Glacier, Northern Victoria Land. Antarct Miner 10:892. https://doi.org/10.3390/min10100892

Kurbatov AV, Zielinski GA, Dunbar NW, Mayewski PA, Meyerson EA, Sneed SB, Taylor KC (2006) A 12,000 year record of explosive volcanism in the Siple Dome Ice Core, West Antarctica. J Geophys Res Atmos 111:D12307. https://doi.org/10.1029/2005JD006072

LeBas MJL, Maitre RWL, Streckeisen A, Zanettin B, IUGS Subcommission on the Systematics of Igneous Rocks (1986) A chemical classification of volcanic rocks based on the total alkali-silica diagram. J Petrol 27:745–750. https://doi.org/10.1093/petrology/27.3.745

Lee MJ, Kyle PR, Iverson NA, Lee JI, Han Y (2019) Rittmann volcano, Antarctica as the source of a widespread 1252 ± 2 CE tephra layer in Antarctica ice. Earth Planet Sci Lett 521:169–176. https://doi.org/10.1016/j.epsl.2019.06.002

Lin SP, Reitz RD (1998) Drop and spray formation from a liquid jet. Ann Rev Fluid Mech 30:85–105. https://doi.org/10.1146/annurev.fluid.30.1.85

Lowe DJ (2011) Tephrochronology and its application: a review. Quat Geochronol 6:107–153. https://doi.org/10.1016/j.quageo.2010.08.003

Lyon GL (1986) Stable isotope stratigraphy of ice cores and the age of the last eruption at Mount Melbourne, Antarctica. New Zeal J Geol Geophys 29:135–138. https://doi.org/10.1080/00288306.1986.10427528

McDonough WF, Sun S-S (1995) The composition of the Earth. Chem Geol 120:223–253. https://doi.org/10.1016/0009-2541(94)00140-4

Morrissey M, Zimanowski B, Wohletz K, Buettner R (2000) Phreatomagmatic fragmentation. In: Sigurdsson H, Houghton B, McNutt SR, Rymer H, Stix J (eds) Encyclopedia of volcanoes. Academic, London, pp 431–445

Narcisi B, Petit JR, Delmonte B, Basile-Doelsch I, Maggi V (2005) Characteristics and sources of tephra layers in the EPICA-Dome C ice record (East Antarctica): implications for past atmospheric circulation and ice core stratigraphic correlations. Earth Planet Sci Lett 239:253–265. https://doi.org/10.1016/j.epsl.2005.09.005

Narcisi B, Petit JR, Delmonte B, Scarchilli C, Stenni B (2012) A 16,000-yr tephra framework for the Antarctic ice sheet: a contribution from the new Talos Dome core. Quat Sci Rev 49:52–63. https://doi.org/10.1016/j.quascirev.2012.06.011

Narcisi B, Petit JR (2021) Chapter 6.2 Englacial tephras of East Antarctica. Geol Soc London, Mem 55:649 LP-664. https://doi.org/10.1144/M55-2018-86

Nardin R, Severi M, Amore A, Becagli S, Burgay F, Caiazzo L, Ciardini V, Dreossi G, Frezzotti M, Hong S-B, Khan I, Narcisi BM, Proposito M, Scarchilli C, Selmo E, Spolaor A, Stenni B, Traversi R (2021) Dating of the GV7 East Antarctic ice core by high-resolution chemical records and focus on the accumulation rate variability in the last millennium. Clim past 17:2073–2089. https://doi.org/10.5194/cp-17-2073-2021

Panter KS (2021) Antarctic volcanism: petrology and tectonomagmatic overview. Geol Soc Lond Mem 55:43–53. https://doi.org/10.1144/M55-2020-10

Peccerillo A, Taylor SR (1976) Geochemistry of eocene calc-alkaline volcanic rocks from the Kastamonu area, Northern Turkey. Contrib Miner Petrol 58:63–81. https://doi.org/10.1007/BF00384745

Rocchi S, Smellie JL (2021) Chapter 5.1b Northern Victoria Land: petrology. Geol Soc London Mem 55:383 LP – 413. https://doi.org/10.1144/M55-2019-19

Ross P-S, Dürig T, Comida PP, Lefebvre N, White JDL, Andronico D, Thivet S, Eychenne J, Gurioli L (2022) Standardized analysis of juvenile pyroclasts in comparative studies of primary magma fragmentation; 1. Overview and Workflow. Bull Volcanol 84:13. https://doi.org/10.1007/s00445-021-01516-6

Severi M, Udisti R, Becagli S, Stenni B, Traversi R (2012) Volcanic synchronisation of the EPICA-DC and TALDICE ice cores for the last 42 kyr BP. Clim past 8:509–517. https://doi.org/10.5194/cp-8-509-2012

Shane P, Hoverd J (2002) Distal record of multi-sourced tephra in Onepoto Basin, Auckland, New Zealand: implications for volcanic chronology, frequency and hazards. Bull Volcanol 64:441–454. https://doi.org/10.1007/s00445-002-0217-2

Shane P, Martin SB, Smith VC, Beggs KF, Darragh MB, Cole JW, Nairn IA (2007) Multiple rhyolite magmas and basalt injection in the 17.7 ka Rerewhakaaitu eruption episode from Tarawera volcanic complex. New Zealand J Volcanol Geotherm Res 164:1–26. https://doi.org/10.1016/j.jvolgeores.2007.04.003

Shane P, Nairn IA, Smith VC, Darragh M, Beggs K, Cole JW (2008) Silicic recharge of multiple rhyolite magmas by basaltic intrusion during the 22.6 ka Okareka Eruption Episode, New Zealand. LITHOS 103:527–549. https://doi.org/10.1016/j.lithos.2007.11.002

Smellie JL (1999) The upper Cenozoic tephra record in the south polar region: a review. Glob Planet Change 21:51–70. https://doi.org/10.1016/S0921-8181(99)00007-7

Smellie JL, Rocchi S, Di Vincenzo G (2023) Controlling influence of water and ice on eruptive style and edifice construction in the Mount Melbourne Volcanic Field (northern Victoria Land, Antarctica). Front Earth Sci - Volcanol 10:1061515. https://doi.org/10.3389/feart.2022.1061515

Smellie JL, Rocchi S (2021) Northern Victoria Land: volcanology. Geological Society, London, Memoirs, 55. https://doi.org/10.1144/M55-2018-60

Tomlinson EL, Thordarson T, Müller W, Thirlwall M, Menzies MA (2010) Microanalysis of tephra by LA-ICP-MS - strategies, advantages and limitations assessed using the Thorsmörk ignimbrite (Southern Iceland). Chem Geol 279:73–89. https://doi.org/10.1016/j.chemgeo.2010.09.013

Wolff EW, Barbante C, Becagli S, Bigler M, Boutron CF, Castellano E, de Angelis M, Federer U, Fischer H, Fundel F, Hansson M, Hutterli M, Jonsell U, Karlin T, Kaufmann P, Lambert F, Littot GC, Mulvaney R, Röthlisberger R, Ruth U, Severi M, Siggaard-Andersen ML, Sime LC, Steffensen JP, Stocker TF, Traversi R, Twarloh B, Udisti R, Wagenbach D, Wegner A (2010) Changes in environment over the last 800,000 years from chemical analysis of the EPICA Dome C ice core. Quat Sci Rev 29(1–2):285–295. https://doi.org/10.1016/j.quascirev.2009.06.013

Zimanowski B, Büttner R, Delino P, White JDL, Wohletz K (2015) Magma-water interaction and phreatomagmatic fragmentation. In: Sigurdsson H, Houghton B, McNutt SR, Rymer H, Stix J (eds) Encyclopedia of Volcanoes, 2nd edn. Academic Press, London, pp 473–484